Title

A multi-slice simulation algorithm for grazing-incidence small-angle X-ray scattering

Journal

Journal of Applied Crystallography, 49(6)

ISSN

0021-8898

Authors

Venkatakrishnan, SV
Donatelli, Jeffrey
Kumar, Dinesh
et al.

Publication Date

2016-12-01

DOI

10.1107/s1600576716013273

Peer reviewed

JOURNAL OF APPLIED CRYSTALLOGRAPHY

ISSN 1600-5767

Received 17 March 2016
Accepted 18 August 2016

Edited by G. Renaud, CEA-Grenoble DSM/INAC/SP2M/NRS, Grenoble, France

Keywords: grazing-incidence small-angle X-ray scattering; GISAXS; distorted-wave Born approximation; multi-slice algorithm.

A multi-slice simulation algorithm for grazing-incidence small-angle X-ray scattering

S. V. Venkatakrishnan,[a] Jeffrey Donatelli,[b] Dinesh Kumar,[a] Abhinav Sarje,[b] Sunil K. Sinha,[c] Xiaoye S. Li[b] and Alexander Hexemer[a]*

[a]Advanced Light Source, Lawrence Berkeley National Laboratory, Berkeley, California, USA, [b]Computational Research Division, Lawrence Berkeley National Laboratory, Berkeley, California, USA, and [c]Department of Physics, University of California, San Diego, California, USA. *Correspondence e-mail: ahexemer@lbl.gov

Grazing-incidence small-angle X-ray scattering (GISAXS) is an important technique in the characterization of samples at the nanometre scale. A key aspect of GISAXS data analysis is the accurate simulation of samples to match the measurement. The distorted-wave Born approximation (DWBA) is a widely used model for the simulation of GISAXS patterns. For certain classes of sample such as nanostructures embedded in thin films, where the electric field intensity variation is significant relative to the size of the structures, a multi-slice DWBA theory is more accurate than the conventional DWBA method. However, simulating complex structures in the multi-slice setting is challenging and the algorithms typically used are designed on a case-by-case basis depending on the structure to be simulated. In this paper, an accurate algorithm for GISAXS simulations based on the multi-slice DWBA theory is presented. In particular, fundamental properties of the Fourier transform have been utilized to develop an algorithm that accurately computes the average refractive index profile as a function of depth and the Fourier transform of the portion of the sample within a given slice, which are key quantities required for the multi-slice DWBA simulation. The results from this method are compared with the traditionally used approximations, demonstrating that the proposed algorithm can produce more accurate results. Furthermore, this algorithm is general with respect to the sample structure, and does not require any sample-specific approximations to perform the simulations.

1. Introduction

Grazing-incidence small-angle X-ray scattering (GISAXS) (Levine *et al.*, 1989) is a well established technique for probing the structure of nanomaterials (Müller-Buschbaum, 2003, 2013; Renaud *et al.*, 2009; Hexemer & Müller-Buschbaum, 2015). Accurate simulations play an important role in the analysis of experimental GISAXS data. GISAXS simulations are usually based on the distorted-wave Born approximation (DWBA) theory (Sinha *et al.*, 1988; Lazzari *et al.*, 2007; Renaud *et al.*, 2009). However, in the case of nanostructures embedded in thin films, there can be a significant variation in the electric field intensity (EFI) within the film (Wang *et al.*, 1992; Narayanan *et al.*, 2005; Babonneau *et al.*, 2009; Jiang *et al.*, 2011), resulting in a depth-dependent enhancement or reduction of the scattering intensity (also referred to as the waveguide effect). Such cases typically occur when the incidence angle of the X-ray beam is greater than the critical angle of the film but smaller than that of the substrate. Furthermore, the EFI is affected by local variations in electron density within the sample, which can be significant for densely packed objects (Lazzari *et al.*, 2007). It has been shown that, in such cases, a more accurate simulation model is one based on the

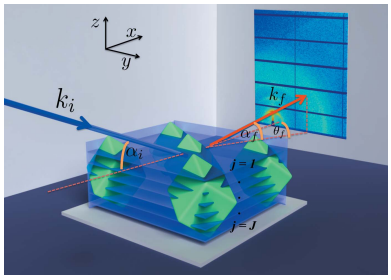

'multi-slice' DWBA (Babonneau *et al.*, 2009; Jiang *et al.*, 2011). In the multi-slice simulation method, the sample is first divided horizontally into multiple slices and an electron-density profile, based on the average refractive index, is computed for each slice. In addition, the Fourier transform (FT) of the structures that intersect with each slice is computed. The contributions from all slices are then combined coherently to obtain the overall scattering pattern (Jiang *et al.*, 2011). Thus, the theory for simulating GISAXS patterns, even under a varying EFI, is reasonably well established.

A number of software tools have been developed for simulation of GISAXS patterns based on the DWBA (Lazzari, 2002; Babonneau, 2010; Sarje *et al.*, 2012; Chourou *et al.*, 2013; Durniak *et al.*, 2015; Jiang, 2015). While some of these (Lazzari, 2002; Babonneau, 2010; Chourou *et al.*, 2013; Durniak *et al.*, 2015) allow simulations of multilayered systems, they do not support cases when the structure size is large or the structure has arbitrary rotations under the condition of a significantly varying EFI. In this paper, an object is defined as a three-dimensional geometric form composed of a single closed domain. A structure is defined as a collection of objects arranged in a periodic (or pseudo-periodic) lattice within a finite region of space (specified by a finite number of object repetitions). The traditional method of addressing the challenge of simulating patterns under the multi-slice DWBA is to approximate the structure within each slice by a simpler object and then compute the GISAXS pattern (Lazzari, 2002; Jiang *et al.*, 2011; Chourou *et al.*, 2013). For example, the simulation of a sphere can be carried out by approximating it with a stack of discs of varying radii (Jiang *et al.*, 2011). However, in some cases this approach can lead to significant discretization errors, while in others it may not be straightforward to apply such approximations. Furthermore, using simpler objects to approximate larger structures is not general enough for the full range of possible objects that a generic simulation algorithm requires. In summary, current numerical approaches for GISAXS simulations do not allow for modeling certain complex structures using the multi-slice DWBA method.

In this paper, we propose an accurate algorithm, termed MAGIXS (multi-slice algorithm for grazing-incidence X-ray scattering simulations), for simulating arbitrary structures using the multi-slice DWBA theory. We use the properties of the FT to evaluate the average refractive index of each slice as well as the FT of the structure that intersects with a given slice. The key advantage of this approach is that it is agnostic to the specifics of the structure that intersects with a slice and can be implemented on the basis of the FT of the overall structure. In particular, we use the property that the area profile of a three-dimensional object along a certain axis can be obtained by computing its FT along that axis with the other components set to zero. This gives a simple method for computing the electron-density profile as a function of the slice. In order to compute the FT of the structure that intersects with a given slice, we use the convolution property of the FT. In particular, the FT at a single point in momentum transfer space is computed *via* a convolution between the FT of the full structure and a window function that is computed depending upon the imaginary part of the momentum transfer vector. Using the proposed ideas, we can accurately simulate any sample geometry in the multi-slice DWBA regime.

We note that, while the DWBA is widely used, the method is still an approximation based on a perturbation theory model (Renaud *et al.*, 2009). Clearly, a more accurate physical model will overcome the assumptions made by the multi-slice DWBA. In this paper, we present a numerically accurate and general algorithm to simulate structures under the assumptions of DWBA physics, which is itself 'approximate'.

We demonstrate *via* simulations of certain test objects that the proposed method is generic and accurate, and that it can outperform alternative approaches. The organization of the rest of this paper is as follows. In §2 we review the multi-slice DWBA approach. In §3 we present the proposed algorithm for the multi-slice DWBA. In §4 we present our results and in §5 we draw our conclusions.

2. Review of multi-slice DWBA

In this section, we summarize the multi-slice DWBA method (Jiang *et al.*, 2011). We assume a GISAXS simulation using an X-ray beam of wavelength λ, incident at an angle α_i relative to the sample. We are interested in simulating the scattering pattern at each output angle (α_f, θ_f), as shown in Fig. 1. The output points can be converted to momentum transfer (q) space using the relation

$$\begin{pmatrix} q_x \\ q_y \\ q_z \end{pmatrix} = k_0 \begin{bmatrix} \cos(\alpha_f)\cos(\theta_f) - \cos(\alpha_i) \\ \sin(\theta_f)\cos(\alpha_f) \\ \sin(\alpha_f) + \sin(\alpha_i) \end{bmatrix}, \qquad (1)$$

where $k_0 = 2\pi/\lambda$.

If the sample is divided into J slices, then the scattered intensity at a point $q = (q_x, q_y, q_z)$ can be written as a summation over all slices as follows:

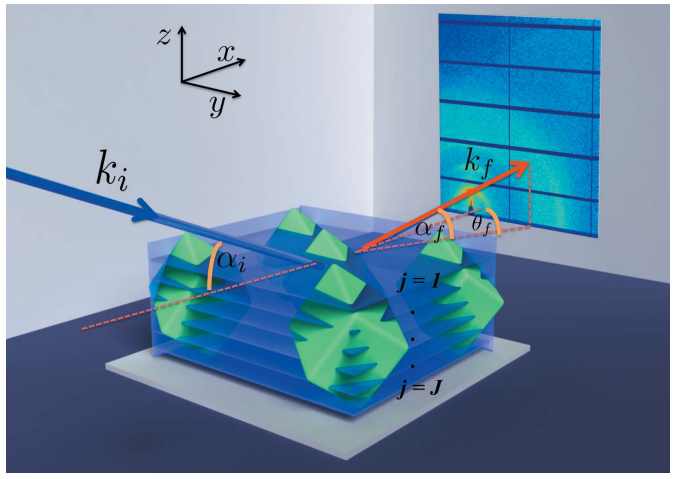

Figure 1
Illustration of the setup used for GISAXS experiments. For simulating this sample, the structure is sliced along the vertical direction and the contributions from each slice are combined to obtain the overall intensity.

$$I(q) \propto \left\langle \left| \sum_{j=1}^{J} \sum_{m=1}^{4} D_j^m(\alpha_i, \alpha_f) \Delta\rho_j F_j\left(q_{||}, q_{z,j}^m\right) \right|^2 \right\rangle, \qquad (2)$$

where $q_{||} = (q_x, q_y)$, F_j is the Fourier transform (FT) of the structure within the jth slice, $\Delta\rho_j = (n_{j,\mathrm{obj}}^2 - n_{j,\mathrm{film}}^2)$, where $n_{j,\mathrm{obj}}$ is the refractive index of the object and $n_{j,\mathrm{film}}$ is that of the film (Jiang *et al.*, 2011), $D_j^m(\alpha_i, \alpha_f)$ are the DWBA coefficients for $m \in \{1, 2, 3, 4\}$ and angle brackets $\langle\ \rangle$ represent the expected value, *i.e.* the mean value averaged over the size, shape and orientation distributions. For the purposes of this paper, we assume a local monodisperse approximation (Jiang *et al.*, 2011) and that we can simulate the expected value *via* a stochastic/Monte Carlo sampling using a large number of 'grains', as described by Chourou *et al.* (2013). A grain is the combination of the structure along with the film and underlying substrate. Note that the coefficients $D_j^m(\alpha_i, \alpha_f)$ are given by

$$\begin{aligned} D_j^1(\alpha_i, \alpha_f) &= T_j^i T_j^f, \\ D_j^2(\alpha_i, \alpha_f) &= T_j^i R_j^f, \\ D_j^3(\alpha_i, \alpha_f) &= R_j^i T_j^f, \\ D_j^4(\alpha_i, \alpha_f) &= R_j^i R_j^f, \end{aligned} \qquad (3)$$

where T and R are the transmitted and reflected wave amplitudes, respectively, computed using Parratt's recursion (Parratt, 1954) and the average refractive index $\bar{n}_j$ of each of the J slices. The EFI due to the incident beam in the jth slice is given by $|T_j^i \exp(-ik_{z,j}^i z_j) + R_j^i \exp(ik_{z,j}^i z_j)|^2$ (Jiang *et al.*, 2011), where $k_{z,j}^i$ is the z component of the incident wavevector in slice j and z_j is the depth of the jth slice interface. The values of $q_{z,j}^m$ in equation (2) correspond to the four scattering events

$$\begin{aligned} q_{z,j}^1 &= k_{z,j}^f - k_{z,j}^i, \\ q_{z,j}^2 &= -k_{z,j}^f - k_{z,j}^i, \\ q_{z,j}^3 &= k_{z,j}^f + k_{z,j}^i, \\ q_{z,j}^4 &= -k_{z,j}^f + k_{z,j}^i. \end{aligned} \qquad (4)$$

Here $k_{z,j}^f = k_0[\sin^2(\alpha_f) + (\bar{n}_j^2 - 1)]^{1/2}$ and $k_{z,j}^i = -k_0[\sin^2(\alpha_i) + (\bar{n}_j^2 - 1)]^{1/2}$. Note that $q_{z,j}^m$ can be a complex number (Babonneau *et al.*, 2009).

Typically, equation (2) is implemented by approximating the structure that intersects with a slice by a simple shape (Jiang *et al.*, 2011) or by assuming that the structures are small with respect to the EFI variation (Babonneau *et al.*, 2009), leading to a simple expression for F_j. The average refractive index is obtained in an approximate manner or is computed manually on a case-by-case basis in order to compute the T and R values for each slice and at each exit angle. While these methods work well for certain cases, as illustrated by Babonneau *et al.* (2009) and Jiang *et al.* (2011), such approximations do not hold for complex cases in which a structure intersecting with a given slice cannot be easily approximated (see, for example, Fig. 2). Next, we present an accurate and generic algorithm to address these challenges.

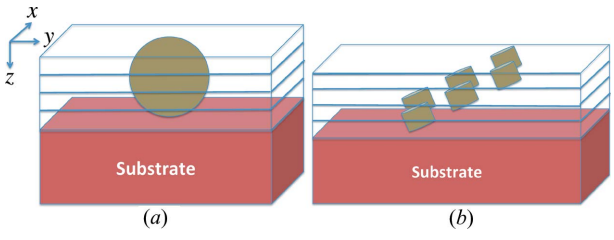

Figure 2
Illustration of cases that are challenging to simulate in the multi-slice framework. One approach would be to approximate the object using simpler structures (like discs) in each slice. However, this will not be applicable in cases like (*b*). Hence there is a need to develop an algorithm to simulate such structures.

3. MAGIXS – a multi-slice algorithm for grazing-incidence X-ray scattering simulations

In this section, we propose an algorithm to implement equation (2) using properties of the FT. First, we compute the average refractive index of a given arbitrary structure as a function of depth (z axis), which allows us to compute D_j^m. We assume that the top of the sample is at $z = 0$ and the sample extends downwards. It is typical to model the structure by an indicator function f that is defined to be 1 inside an object and zero elsewhere (Jiang *et al.*, 2011). If $f(x, y, z)$ is an indicator function for the structure, then the cross section with respect to the z axis is

$$A(z) = \int\int f(x, y, z)\, \mathrm{d}x\, \mathrm{d}y. \qquad (5)$$

In a typical simulation, explicitly constructing f and evaluating equation (5) is computationally expensive. Instead, we often have simple expressions for the FT of the structure (for example, a collection of spheres in a regular lattice). To

Input: FT of sample F, ref. indices, coherent area, Exp. params $(\alpha_i, \alpha_f, \theta_f)$, number of slices J, FT resolution Δ
Output: Simulated Intensity $I(q)$
$I(q) = 0$
Compute Fourier transform of object $F(0, 0, l\Delta)$ for all l for a fixed resolution Δ
Compute average refractive index of each slice $\bar{n}$ using (5)
$(T^i, R^i) \leftarrow$PARRATT$(\alpha_i, \lambda, \bar{n})$
for Each exit angle α_f **do**
  $(T^f, R^f) \leftarrow$ PARRATT$(\alpha_f, \lambda, \bar{n})$
  for $m = 1$ to 4 **do**
    Compute DWBA amplitude, $D_j^m(\alpha_i, \alpha_f)$, using (3) based on $T_j^i, R_j^i, T_j^f, T_j^f$
  end for // *Wave amplitudes for all slices*
end for
for Each $q = (q_{||}, q_z)$ **do**
  Compute $F(q_{||}, l\Delta)$ for all l
  for $j = 1$ to J **do**
    Compute $\Delta\rho_j$
    for $m = 1$ to 4 **do**
      Compute required complex z frequency $(q_{z,j}^{m,R} + iq_{z,j}^{m,I})$
      Evaluate the window function $\tilde{W}_j(q_{z,j}^{m,R} - l\Delta; q_{z,j}^{m,I})$ for all l
      Compute $F_j(q_{||}, q_{z,j}^m)$ using (11)
      $I(q) += \Delta\rho_j * D_j^m(\alpha_i, \alpha_f) F_j(q_{||}, q_{z,j}^m)$
    end for
  end for
  $I(q) \leftarrow |I(q)|^2$
end for

Figure 3
Pseudo-code of the MAGIXS algorithm.

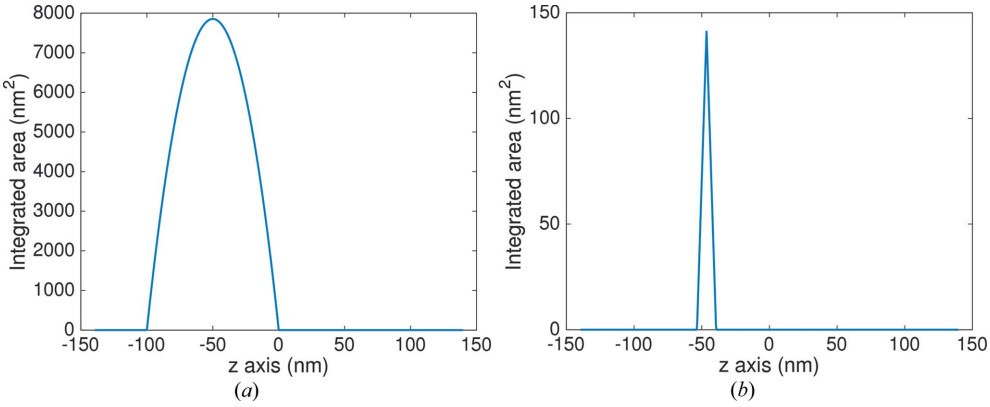

Figure 4
Area profiles derived from the Fourier transform at $q_x = q_y = 0$ for (*a*) a sphere of radius 50 nm and (*b*) a cube of side 10 nm rotated by 45°. Both objects are embedded inside a film of thickness 100 nm. The convention is that the top of the film is at $z = 0$ and the bottom is at $z = -100$ nm.

compute the area profile efficiently using Fourier transforms, note that

$$\begin{aligned} F(q_x, q_y, q_z) &= \int\int\int f(x, y, z) \\ &\quad \times \exp\left[-i\left(xq_x + yq_y + zq_z\right)\right] \mathrm{d}x\, \mathrm{d}y\, \mathrm{d}z, \\ F(0, 0, q_z) &= \int\int\int f(x, y, z)\, \mathrm{d}x\, \mathrm{d}y \exp\left(-izq_z\right) \mathrm{d}z \\ &= \int A(z) \exp\left(-izq_z\right) \mathrm{d}z \\ \text{and} \quad A(z) &= \frac{1}{2\pi} \int F(0, 0, q_z) \exp\left(iq_z z\right) \mathrm{d}q_z, \end{aligned} \tag{6}$$

where F is the FT of f. Hence, the area profile is simply obtained by a one-dimensional inverse FT of the structure's three-dimensional FT evaluated along $q_x = 0$ and $q_y = 0$. Normalizing $A(z)$ by the area of the grain along the xy plane, A_{coh}, gives us the volume fraction of the structure at any given depth. This can be used to compute the average refractive index $\overline{n}$ using the expression

$$\overline{n}(z) = n_{\mathrm{obj}} \frac{A(z)}{A_{\mathrm{coh}}} + n_{\mathrm{film}} \left[1 - \frac{A(z)}{A_{\mathrm{coh}}}\right], \tag{7}$$

where n_{obj} is the refractive index of the object and n_{film} is that of the film. The values of $\overline{n}(z)$ can then be discretized and used to compute the D_j^m in equation (2) using Parratt's recursion (Parratt, 1954).

The next step is to compute F_j, the Fourier transform of the structure in the jth slice at a value $(q_{||}, q_{z,j}^m)$, from the full three-dimensional FT of the structure. In contrast with approximating the intersection of the structure and a given slice with a 'simple' shape (or collection of shapes), which can be challenging in the general case, we propose computing this quantity *via* a convolution. The intersection of the structure with the jth slice in real space can be computed *via* the multiplication of the indicator function and a window function, *i.e.* $f_j(x, y, z) = f(x, y, z)\, w_j(x, y, z)$, where w_j is given by

$$w_j(x, y, z) = \begin{cases} 1 & -j\Delta_{\mathrm{s}} < z < -(j-1)\Delta_{\mathrm{s}}, \\ 0 & \text{otherwise}, \end{cases} \tag{8}$$

and Δ_{s} is the thickness of each slice. Note that w_j is an indicator function that selects the jth slice. This model can easily be extended to account for non-uniform slice thicknesses. Using the definition of w_j, the Fourier transform of f_j at a given q is

$$F_j(q_{||}, q_z) = \left(F * * * \widehat{W}_j\right)(q_{||}, q_z), \tag{9}$$

where $\widehat{W}_j(q_{||}, q_z) = \delta(q_{||})\Delta_{\mathrm{s}} \mathrm{sinc}(\Delta_{\mathrm{s}} q_z/2) \exp[i\,(j - \frac{1}{2})\Delta_{\mathrm{s}} q_z]$ is the FT of w_j, $\mathrm{sinc}(t) = \sin(t)/t$ and *** denotes three-dimensional convolution. Substituting the FT of w_j from equation (8), we get the FT of the structure in the jth slice as

$$F_j(q_{||}, q_{z,j}^m) = \left[F(q_{||}, .) * W_j\right](q_{z,j}^m), \tag{10}$$

where $W_j(q_z) = \Delta_{\mathrm{s}} \mathrm{sinc}(\Delta_{\mathrm{s}} q_z/2) \exp[-i\,(j - \frac{1}{2})\Delta_{\mathrm{s}} q_z]$. While this is straightforward to implement *via* one-dimensional convolutions when $q_{z,j}^m$ is real, it is not so in general when $q_{z,j}^m$ is complex, as discussed in §2. To address the issue of complex

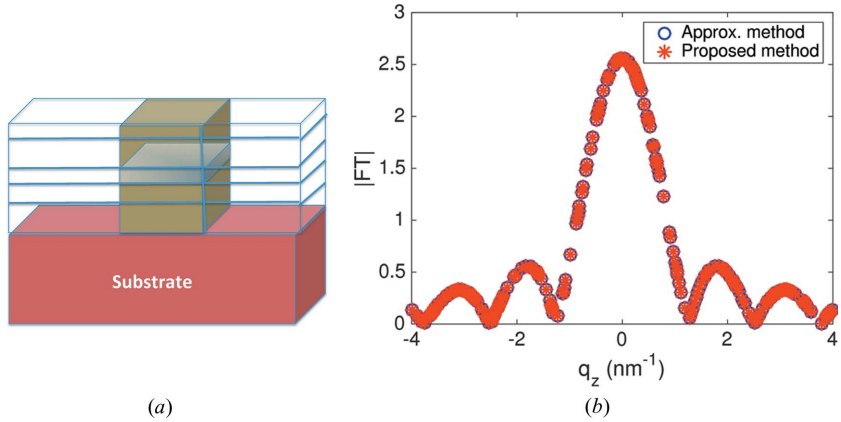

Figure 5
(*b*) Comparison of the FT of a box [shown in part (*a*)] along the real part of q_z for fixed $q_{||} = 1$ nm^{-1} and $q_z^1 = -0.1$ nm^{-1} by direct implementation and *via* Fourier domain convolution. In the case of a box, the sliced FT can be computed analytically. We compare this analytical solution with the one obtained by the proposed convolution-based approach. This provides confirmation of the correctness of the proposed method.

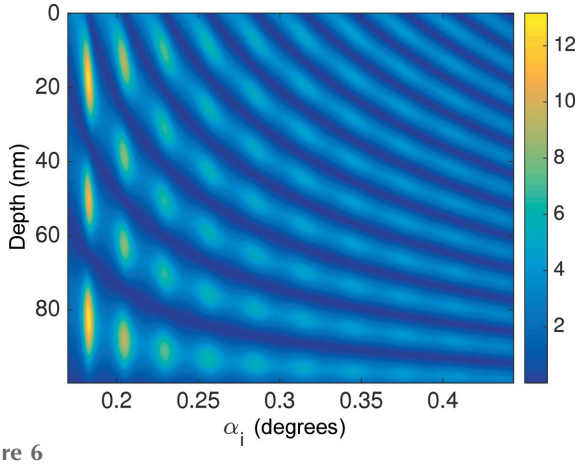

Figure 6
The simulated electric field intensity (EFI) inside a 100 nm thick film containing a single sphere of radius 50 nm, plotted as a function of depth for different incident angles. The average refractive index is computed using the proposed method. Note that, at certain depths, there are peaks in the EFI leading to an enhancement of the scattering intensity.

$q^m_{z,j}$, we simplify the expression and use $q^m_{z,j} = q^{m,\mathrm{R}}_{z,j} + iq^{m,\mathrm{I}}_{z,j}$ to rewrite the definition of the FT as

$$\begin{aligned} F_j(q_{||}, q^m_{z,j}) &= \int\int f(r_{||}, z) w_j(r_{||}, z) \\ &\quad \times \exp\{-i[q^{\mathrm{t}}_{||} r_{||} + (q^{m,\mathrm{R}}_{z,j} + iq^{m,\mathrm{I}}_{z,j})z]\}\, \mathrm{d}r_{||}\, \mathrm{d}z \\ &= \int\int f(r_{||}, z) w_j(r_{||}, z) \\ &\quad \times \exp[(q^{m,\mathrm{I}}_{z,j} z)] \exp[-i(q^{\mathrm{t}}_{||} r_{||} + q^{m,\mathrm{R}}_{z,j} z)]\, \mathrm{d}r_{||}\, \mathrm{d}z \\ &= \int\int f(r_{||}, z) \widetilde{w}_j(r_{||}, z\,;\, q^{m,\mathrm{I}}_{z,j}) \\ &\quad \times \exp[-i(q^{\mathrm{t}}_{||} r_{||} + q^{m,\mathrm{R}}_{z,j} z)]\, \mathrm{d}r_{||}\, \mathrm{d}z \\ &= \left[F(q_{||}, .) * \widetilde{W}_j(.\,;\, q^{m,\mathrm{I}}_{z,j})\right](q^{m,\mathrm{R}}_{z,j}), \end{aligned} \tag{11}$$

where the superscript t refers to the transpose operator, $r_{||} = (x, y)$ is a column vector, the integral with respect to $r_{||}$ represents a double integral, $\widetilde{w}_j(r_{||}, z\,;\, q^{m,\mathrm{I}}_{z,j}) = w_j(r_{||}, z) \times \exp(q^{m,\mathrm{I}}_{z,j} z)$ and $\widetilde{W}_j$ is the one-dimensional FT of $\widetilde{w}_j$ evaluated at the appropriate frequency. Furthermore, we have used the convolution property of FTs in the last line of the above equation. Thus, the new window function in Fourier space, $\widetilde{W}_j$, for a given $q^m_{z,j}$ is the FT of a rectangular window modulated by an exponential function, with the exponent dependent on the imaginary part of $q^m_{z,j}$. Using the definition of the FT, for some a and b, the value of $\widetilde{W}_j$ can be written as

$$\widetilde{W}_j(a\,;\, b) = \frac{\exp[-(j-1)\Delta_s(a-ib)] - \exp[-j\Delta_s(a-ib)]}{a - ib}. \tag{12}$$

Using the definition of convolution,

$$\begin{aligned} F_j(q_{||}, q^m_{z,j}) &= \int_{-\infty}^{\infty} F(q_{||}, \tau) \widetilde{W}_j(q^{m,\mathrm{R}}_{z,j} - \tau\,;\, q^{m,\mathrm{I}}_{z,j})\, \mathrm{d}\tau \\ &\simeq \sum_{l=-L}^{L} F(q_{||}, l\Delta) \widetilde{W}_j(q^{m,\mathrm{R}}_{z,j} - l\Delta\,;\, q^{m,\mathrm{I}}_{z,j})\Delta, \end{aligned} \tag{13}$$

where Δ is the integration step size, L is a large number and we have used a Riemann integration strategy to implement the convolution at the desired point. Thus, the computation of the FT at a given complex $q^m_{z,j}$ is simplified to a one-dimensional convolution that can be implemented numerically.

3.1. Computation

While the above method is exact because it does not approximate the intersection of a structure with a slice, it requires significantly more computations than the traditional approach. The computation of the intensity at each point using the proposed approach requires the evaluation of integrals, instead of simple function evaluations. To implement the simulation efficiently, we utilize graphical processor units (GPUs) and multi-core central processor units (CPUs). The FT of the sample, $F(q_{||}, l\Delta)$, is first evaluated over a fine grid with step size Δ once for each output point and stored in a persistent buffer on the GPU. For each slice j and DWBA component m, this buffer is accessed, the window FT for the complex $q^m_{z,j}$, $\widetilde{W}_j$, is evaluated over the $q^{m,R}_{z,j} - l\Delta$ grid and the integration is performed on the GPU. We note that the numerical integration can be performed more efficiently by using better quadratures, further reducing the computing time.

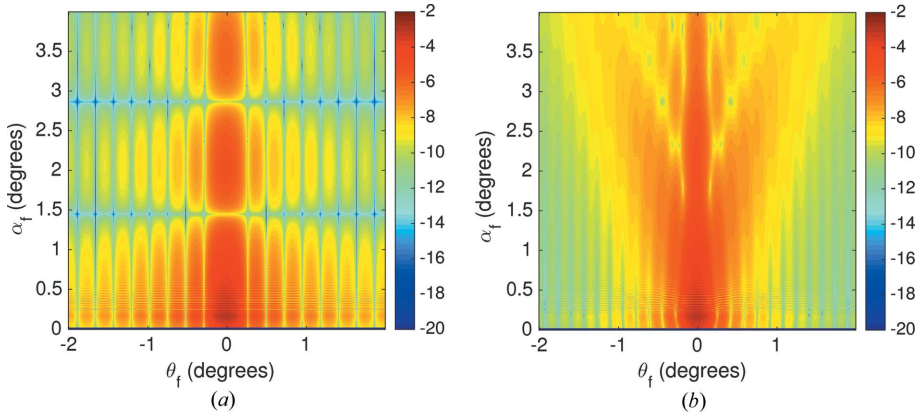

Figure 7
Comparison of simulated GISAXS patterns from the topmost slice of a sphere of radius 50 nm inside a film of thickness 100 nm using $J = 20$ slices. The figure shows simulations of a 5 nm thick sliced section from the top, computed using two methods: (*a*) approximation by a cylinder and (*b*) the method proposed in this paper. Note that the approximation by a cylinder at the top is not accurate owing to the high curvature at the top.

Since the computation of each $(q_{\|}, q_z)$ is independent, we compute these in parallel on a multi-core CPU. The final MAGIXS algorithm is summarized in Fig. 3. In summary, the user has to specify the detector geometry, the sample structure *via* a function to compute its Fourier transform at any point, the number of slices to use and, optionally, the numerical accuracy of the convolution [L and Δ in equation (13)] for a given simulation.

4. Results

In this section, we present results that illustrate how the MAGIXS algorithm improves upon the current state of the art. First, we present results to illustrate the accuracy of the method of computing the average refractive index profile (§4.1), as well as the FT of the structure in a slice (§4.2). Next, we present GISAXS simulations of some illustrative cases to demonstrate the generality of the proposed algorithm (§§4.3 and 4.4). Where appropriate, we compare the proposed method with the traditional method based on approximating a structure by a collection of simpler objects. Unless otherwise specified, for all simulations we assume a 10 keV X-ray beam incident at $\alpha_i = 0.183^\circ$. The output is simulated at 512 × 512 points for $\alpha_f \in [0^\circ, 4^\circ]$ and $\theta_f \in [-2^\circ, 2^\circ]$. The values of dispersion (δ) and absorption (β), respectively, for the sample materials are as follows:

(i) Sample (polymer): 2.67×10^{-6} and 3.71×10^{-9}.

(ii) Film (polymer): 4.41×10^{-6} and 1.40×10^{-8}.

(iii) Substrate (gold): 2.99×10^{-5} and 2.20×10^{-6}.

The value of L for the numerical integration was set so that $2L + 1 = 512^2$ and $\Delta = 0.012$ nm^{-1}. All the simulated GISAXS intensities are displayed on a log scale.

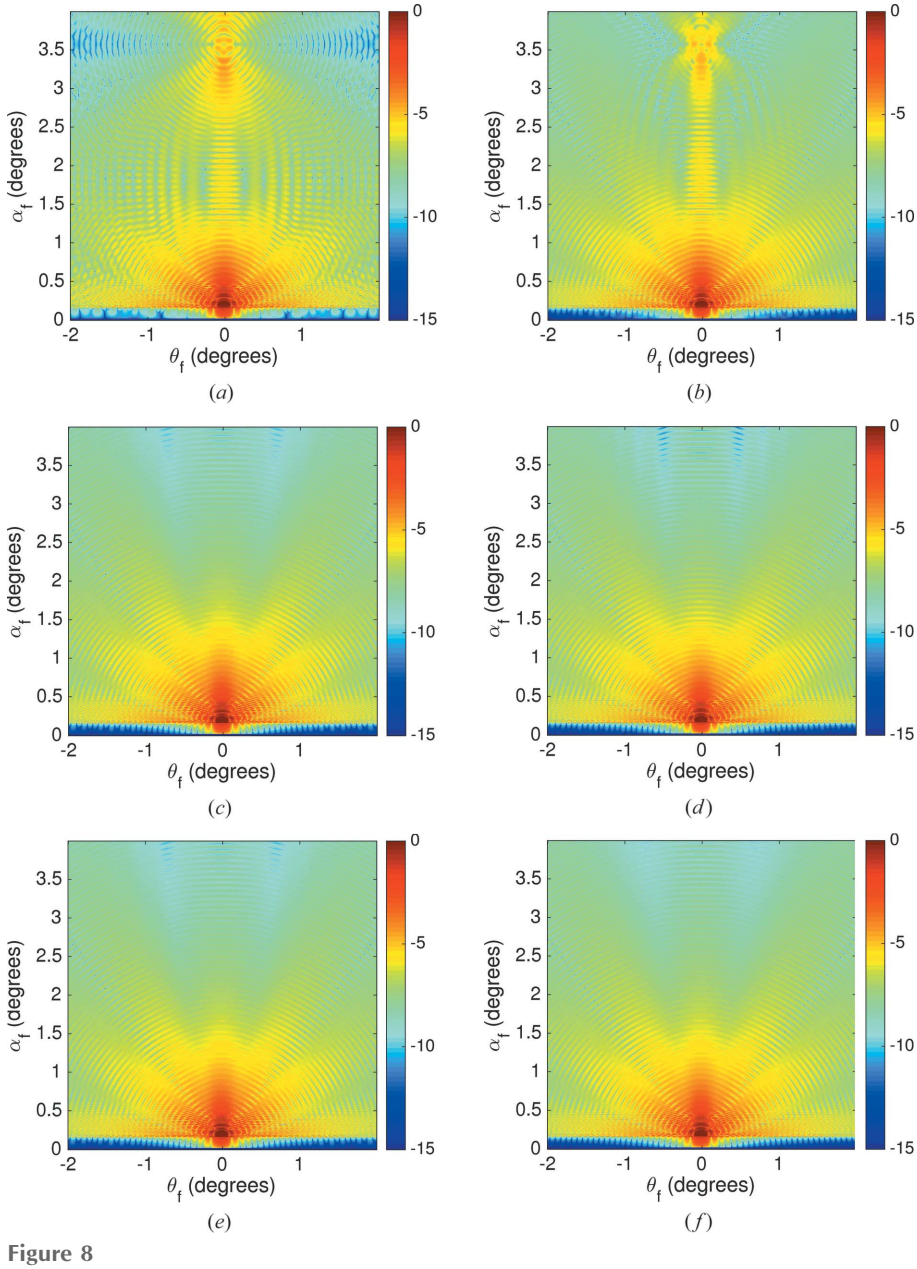

Figure 8
Comparison of simulated GISAXS patterns of a sliced sphere of radius 50 nm inside a film of thickness 100 nm using (*a*), (*c*), (*e*) approximation by discs and (*b*), (*d*), (*f*) the method proposed here, by varying the number of slices *J*. Visually, the proposed algorithm appears to converge to the solution faster than the disc approximation.

4.1. Average refractive index

First, we illustrate the method for obtaining the area profile from the FT of the structure, as discussed in §3. Figs. 4(*a*) and 4(*b*) show the area profile as a function of depth for a sphere, and for a box rotated by 45° with respect to the x axis inside a film of thickness 100 nm, respectively. We note that, by using the inverse FT along the appropriate q range, we can accurately compute the area profile and hence the average refractive index in each slice. No matter how complex the structure, this method can extract the desired refractive index profile of the sample.

4.2. FT *via* convolution

Next, we numerically verify the algorithm for computing the FT of the structure that intersects a given slice at the desired set of (complex) q values. We choose the simple case of a large box inside a film. In this case, the box can be modeled exactly using a stack of smaller boxes (see Fig. 5*a*). Hence the proposed approach should produce the same answer as the 'approximation' approach. In particular, we simulate the FT due to a single slice of the box. Let Δ_s be the size of a slice, and w the width

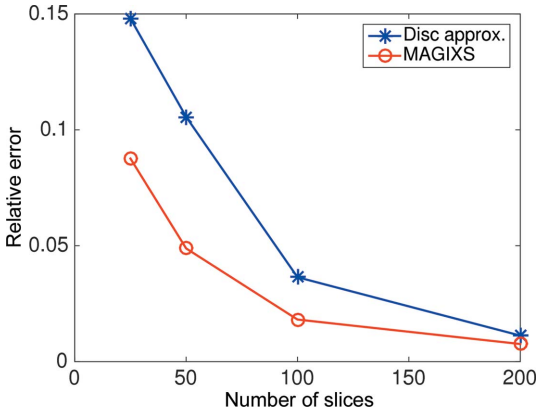

Figure 9
Illustration of the quantitative accuracy of the proposed method for GISAXS simulation of a sphere, plotted as a function of the number of slices. In general, the proposed MAGIXS algorithm has a lower relative error to the 'ground truth' (produced by running $J = 400$) compared with the disc approximation, illustrating the strength of the method. As the number of slices increases, the two methods converge to the same solution. However, the approximation method cannot be used for a general nanostructure.

of the box, H its height and l its length. We consider the jth slice that is centered at a depth d_j. Then the Fourier transform by the 'approximation' method is

$$F_j(q_x, q_y, q_{z,j}^m) = lw\Delta_s \mathrm{sinc}\left(q_x \frac{l}{2}\right)\mathrm{sinc}\left(q_y \frac{w}{2}\right)\mathrm{sinc}\left(q_{z,j}^m \frac{\Delta_s}{2}\right) \times \exp\left(iq_{z,j}^m d_j\right). \quad (14)$$

Alternatively, this can be implemented by the convolution method of equation (13). If $q_{z,j}^m = q_{z,j}^{m,\mathrm{R}} + \mathrm{i}q_{z,j}^{m,\mathrm{I}}$, the FT of the structure is obtained by computing the convolution between

$$F(q_x, q_y, q_{z,j}^{m,\mathrm{R}}) = lwH\mathrm{sinc}\left(q_x \frac{l}{2}\right)\mathrm{sinc}\left(q_y \frac{w}{2}\right)\mathrm{sinc}\left(q_{z,j}^{m,\mathrm{R}} \frac{H}{2}\right) \times \exp\left(iq_{z,j}^{m,\mathrm{R}} \frac{H}{2}\right), \quad (15)$$

and the modified window that depends on $q_{z,j}^{m,\mathrm{I}}$. Fig. 5 shows the absolute value of the FT from the two approaches for a set of 512 randomly chosen points along $q_{z,j}^{m,\mathrm{R}}$, for fixed q_x, q_y and $q_{z,j}^{m,\mathrm{I}}$. Note that the two methods result in answers that are visually indistinguishable. The normalized error between the two approaches over the 512 points is 1×10^{-5}. This verifies the numerical accuracy of the FT in a single slice obtained *via* the convolution approach.

4.3. Simulation: sphere

We illustrate the utility of the MAGIXS algorithm by simulating an embedded sphere of radius 50 nm in a film of thickness 100 nm, where there is significant variation in the EFI along the film depth. The sphere is centered at a depth of 50 nm below the surface of the film. The simulation was performed using two approaches: by approximating the sphere with a stack of discs, and using the MAGIXS algorithm. We also studied the quantitative accuracy of the algorithm by varying the number of slices. In order to have a reference ground truth, we set $J = 400$ and ran the MAGIXS method.

Fig. 6 shows the computed EFI inside the film of this sample across a range of incidence angles. Fig. 7 shows the output intensities (log scale) from the topmost slice of the sphere when $J = 20$ (each slice is 5 nm). Since the curvature is high at the top, the approximation using discs is not accurate, while the MAGIXS method accurately produces the wing-like patterns associated with this shape. This illustrates the advantage of MAGIXS in simulating complex structures.

Fig. 8 shows the simulated patterns due to the full sphere using the two methods by varying the number of slices. Note that the ground truth is best represented by Fig. 8(f). In general, the MAGIXS method approaches the reference solution with fewer slices than the disc approximation technique. This error is quantified in Fig. 9. Thus, the MAGIXS method presents a more accurate algorithm for the simulation compared with the disc approximation approach. However, we note that the computation resources required for the MAGIXS method are significantly higher. Therefore, for the case of simulating simple objects like a sphere, the approximation method with a large number of slices might be good enough for the purposes of analysis. However, unlike the

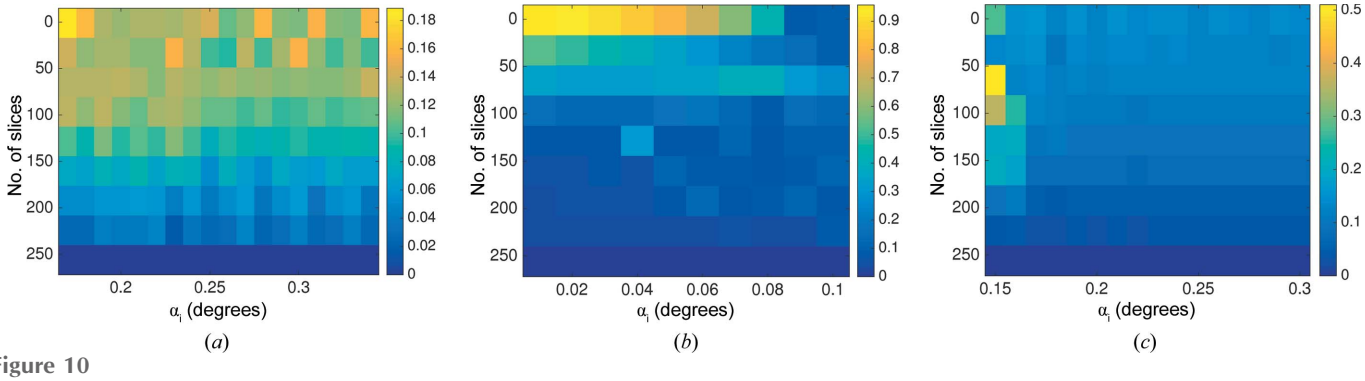

Figure 10
The relative error of the log intensity of the simulations using the MAGIXS algorithm plotted with varying incidence angle for three systems of materials: (a) a polystyrene (PS) sphere embedded in a polymethyl methacrylate (PMMA) matrix on a gold substrate, (b) a PS sphere in air on a gold substrate and (c) a PMMA sphere in a PS film on an Si substrate. Note that the overall error decreases as the number of slices for simulation increases across the range of incidence angles, since the sphere is large.

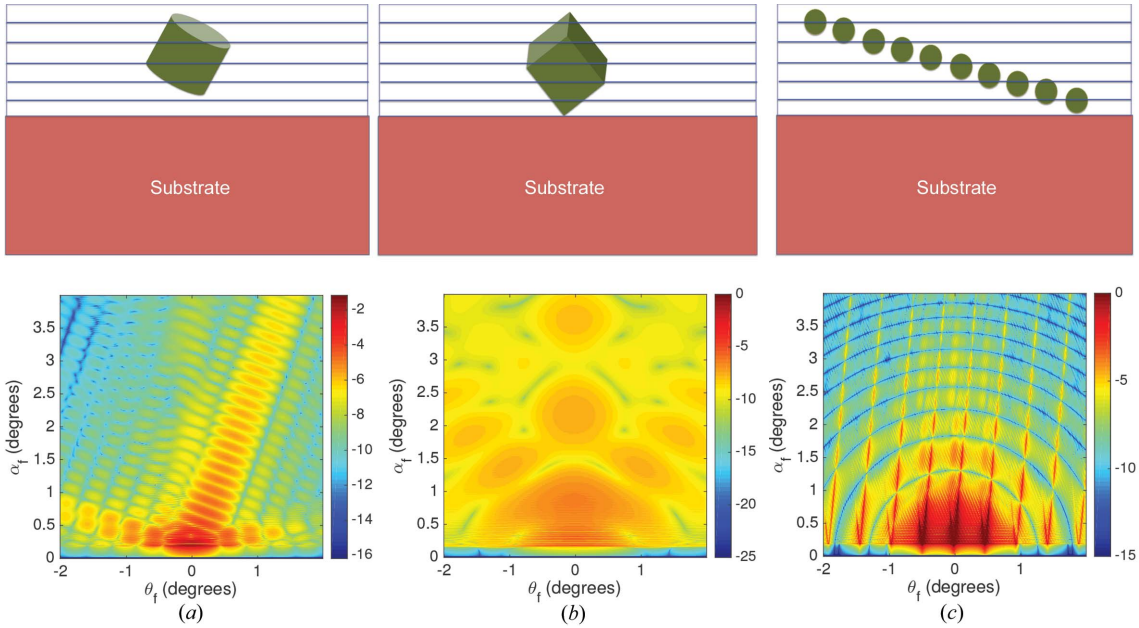

Figure 11
Illustrations of simulations using the MAGIXS algorithm of (*a*) a rotated cylinder, (*b*) a rotated box and (*c*) spheres in a rotated lattice. The MAGIXS method provides an accurate numerical technique to simulate GISAXS patterns from complex geometries.

approximation approach, the MAGIXS algorithm is general because it does not depend on the shape of the object.

The question of when it is appropriate to use a multi-slice simulation was briefly discussed by Jiang *et al.* (2011). In this work, we provide additional numerical experiments illustrating the errors that can occur if a slicing technique with a sufficiently large number of slices is not used. We present results for a single embedded sphere across a range of incidence angles as well as different sample materials. Fig. 10(*a*) shows the log–error plot of the simulated patterns with increasing numbers of slices for the default materials stated earlier. It is interesting to note that, despite there being significant variations in EFI due to the incident beam, the relative error pattern is similar across various incident angles. This observation is consistent with the findings of Jiang *et al.* (2011). A similar pattern is observed across a collection of different materials (see Figs. 10*b* and 10*c*), suggesting that a multi-slice simulation can be accurate in a variety of cases.

4.4. Simulation: complicated structures

In this section, we demonstrate a fundamental strength of the MAGIXS algorithm: the ability to address cases which are difficult, if not impossible, to simulate using existing approaches. We simulate three sample geometries: a rotated cylinder, a rotated box and spheres in a rotated cubic lattice. The objects are rotated around the x direction. The cylinder has a radius of 25 nm and a height of 25 nm, and is rotated about the x axis at an angle of 20°. The box has a dimension of 10 nm in each of the x, y and z directions, and is rotated about the x axis at an angle of 45°. For the spheres in a rotated simple cubic lattice, the radii are all 5 nm, and there are 100 spheres in the x and y directions at a spacing of 15 nm. The lattice is rotated about the x axis by 5°. Fig. 11 shows the output from the three cases using the MAGIXS method.

In each case, the MAGIXS algorithm produces an accurate simulation of the GISAXS patterns. While only three cases are presented here for illustration, we emphasize that MAGIXS can accurately simulate GISAXS patterns for any morphology with rotated objects and rotated lattices, without having to make any kind of approximation.

5. Conclusions

We have presented an accurate and generic algorithm to compute GISAXS patterns from arbitrary structures using the multi-slice DWBA method combined with a local monodisperse approximation. The primary innovation in our approach is to use the properties of the FT to evaluate the average refractive index (electron-density profile), as well as the FT of the structure that intersects with a given slice. We have validated our method using simulations of several nanostructures embedded in thin films. Our algorithm could increase the applicability of the multi-slice method and eventually lead to improved quantitative accuracy of GISAXS fitting routines. In the future, we plan to investigate automated selection of the number of slices in order to minimize the time required for the simulations.

Acknowledgements

SVV and AH were supported by AH's Early Career Award from the US Department of Energy (DoE). The Advanced Light Source is supported by the Director, Office of Science, Office of Basic Energy Sciences, US DoE, under contract No. DE-AC02-05CH11231. This work was partially supported by

the Center for Advanced Mathematics for Energy Research Applications (CAMERA). SKS's work at UCSD was supported by the Office of Basic Energy Sciences, US DoE, under grant No. DE-SC0003678. We thank Yi Yang and Jingjin Song, Department of Physics, University of California San Diego, for helpful discussions.

References

Babonneau, D. (2010). *J. Appl. Cryst.* **43**, 929–936.
Babonneau, D., Camelio, S., Lantiat, D., Simonot, L. & Michel, A. (2009). *Phys. Rev. B*, **80**, 155446.
Chourou, S. T., Sarje, A., Li, X. S., Chan, E. R. & Hexemer, A. (2013). *J. Appl. Cryst.* **46**, 1781–1795.
Durniak, C., Ganeva, M., Pospelov, G., Van Herck, W. & Wuttke, J. (2015). *BornAgain*, http://www.bornagainproject.org.
Hexemer, A. & Müller-Buschbaum, P. (2015). *IUCrJ*, **2**, 106–125.
Jiang, Z. (2015). *J. Appl. Cryst.* **48**, 917–926.
Jiang, Z., Lee, D. R., Narayanan, S., Wang, J. & Sinha, S. K. (2011). *Phys. Rev. B*, **84**, 075440.
Lazzari, R. (2002). *J. Appl. Cryst.* **35**, 406–421.
Lazzari, R., Leroy, F. & Renaud, G. (2007). *Phys. Rev. B*, **76**, 125411.
Levine, J. R., Cohen, J. B., Chung, Y. W. & Georgopoulos, P. (1989). *J. Appl. Cryst.* **22**, 528–532.
Müller-Buschbaum, P. (2003). *Anal. Bioanal. Chem.* **376**, 3–10.
Müller-Buschbaum, P. (2013). *Polym. J.* **45**, 34–42.
Narayanan, S., Lee, D. R., Guico, R. S., Sinha, S. K. & Wang, J. (2005). *Phys. Rev. Lett.* **94**, 145504.
Parratt, L. G. (1954). *Phys. Rev.* **95**, 359–369.
Renaud, G., Lazzari, R. & Leroy, F. (2009). *Surface Sci. Rep.* **64**, 255–380.
Sarje, A., Li, X. S., Chourou, S., Chan, E. R. & Hexemer, A. (2012). *Proceedings of the International Conference on High Performance Computing, Networking, Storage and Analysis*, SC12, pp. 46:1–46:11.
Sinha, S. K., Sirota, E. B., Garoff, S. & Stanley, H. B. (1988). *Phys. Rev. B*, **38**, 2297–2311.
Wang, J., Bedzyk, M. & Caffrey, M. (1992). *Science*, **258**, 775–778.